

Tennessee State University

Digital Scholarship @ Tennessee State University

Information Systems and Engineering
Management Research Publications

Center of Excellence in Information Systems
and Engineering Management

11-30-2021

The Hubble PanCET program: Transit and Eclipse Spectroscopy of the Hot-Jupiter WASP-74b

Guangwei Fu
University of Maryland at College Park

Drake Deming
University of Maryland at College Park

Erin May
Johns Hopkins University Applied Physics Laboratory

Kevin Stevenson
Johns Hopkins University Applied Physics Laboratory

David K. Sing
Johns Hopkins University

See next page for additional authors

Follow this and additional works at: <https://digitalscholarship.tnstate.edu/coe-research>



Part of the [Astrophysics and Astronomy Commons](#)

Recommended Citation

Guangwei Fu et al 2021 AJ 162 271













This Article is brought to you for free and open access by the Center of Excellence in Information Systems and Engineering Management at Digital Scholarship @ Tennessee State University. It has been accepted for inclusion in Information Systems and Engineering Management Research Publications by an authorized administrator of Digital Scholarship @ Tennessee State University. For more information, please contact XGE@Tnstate.edu.

Authors

Guangwei Fu, Drake Deming, Erin May, Kevin Stevenson, David K. Sing, Joshua D. Lothringer, Hannah R. Wakeford, Nikolay Nikolov, Thomas Mikal-Evans, Vincent Bourrier, Leonardo A. dos Santos, Munazza K. Alam, Gregory W. Henry, Antonio García Muñoz, and Mercedes López-Morales



The Hubble PanCET program: Transit and Eclipse Spectroscopy of the Hot-Jupiter WASP-74b

Guangwei Fu¹ , Drake Deming¹, Erin May² , Kevin Stevenson² , David K. Sing³ , Joshua D. Lothringer³ , H. R. Wakeford⁴, Nikolay Nikolov⁵ , Thomas Mikal-Evans⁶ , Vincent Bourrier⁷ , Leonardo A. dos Santos⁷ , Munazza K. Alam^{8,9} , Gregory W. Henry¹⁰ , Antonio García Muñoz¹¹, and Mercedes López-Morales¹² 

¹ Department of Astronomy, University of Maryland, College Park, MD 20742, USA; guangweifu@gmail.com

² Johns Hopkins APL, 11100 Johns Hopkins Road, Laurel, MD 20723, USA

³ Department of Physics and Astronomy, Johns Hopkins University, Baltimore, MD 21218, USA

⁴ School of Physics, University of Bristol, HH Wills Physics Laboratory, Tyndall Avenue, Bristol, BS8 1TL, UK

⁵ Space Telescope Science Institute, 3700 San Martin Drive, Baltimore, MD 21218, USA

⁶ Department of Physics, and Kavli Institute for Astrophysics and Space Research, Massachusetts Institute of Technology, Cambridge, MA, USA

⁷ Observatoire Astronomique de l'Université de Genève, 51 chemin des Maillettes 1290 Versoix, Switzerland

⁸ Department of Astronomy, Center for Astrophysics | Harvard & Smithsonian, 60 Garden Street, Cambridge, MA 02138, USA

⁹ Carnegie Earth & Planets Laboratory, 5241 Broad Branch Road NW, Washington, DC 20015, USA

¹⁰ Tennessee State University, Center of Excellence in Information Systems, Nashville, TN 37209, USA

¹¹ AIM, CEA, CNRS, Université Paris-Saclay, Université de Paris, F-91191 Gif-sur-Yvette, France

¹² Center for Astrophysics | Harvard & Smithsonian, 60 Garden Street, Cambridge, MA 02138, USA

Received 2021 July 13; revised 2021 September 24; accepted 2021 October 8; published 2021 November 30

Abstract

Planets are like children with each one being unique and special. A better understanding of their collective properties requires a deeper understanding of each planet. Here we add the transit and eclipse spectra of hot-Jupiter WASP-74b into the ever growing data set of exoplanet atmosphere spectral library. With six transits and three eclipses using the Hubble Space Telescope and Spitzer Space Telescope (Spitzer), we present the most complete and precise atmospheric spectra of WASP-74b. We found no evidence for TiO/VO nor super-Rayleigh scattering reported in previous studies. The transit shows a muted water feature with strong Rayleigh scattering extending into the infrared. The eclipse shows a featureless blackbody-like WFC3/G141 spectrum and a weak methane absorption feature in the Spitzer 3.6 μm band. Future James Webb Space Telescope follow-up observations are needed to confirm these results.

Unified Astronomy Thesaurus concepts: [Exoplanet atmospheres \(487\)](#); [Exoplanet atmospheric composition \(2021\)](#)

Supporting material: machine-readable tables

1. Introduction

With the many recent studies of hot-Jupiter atmospheres, we are starting to see a highly diverse landscape of atmospheric chemical composition and thermal structure. Some ultrahot ($T_{\text{eq}} > 2000$ K) Jupiters have shown significant gaseous heavy metal absorption (Lothringer et al. 2020; Fu et al. 2021) while other cooler hot Jupiters exhibit high metallicity (Colón et al. 2020; Lewis et al. 2020; Sheppard et al. 2021) and aerosols coverage (Alam et al. 2020). We have also detected absorption and emission features of various chemical species such as water, sodium, CO/CO₂, metals, and metal oxides (TiO and VO; Evans et al. 2017; Kreidberg et al. 2018; Fu et al. 2021). With this ever growing library of exoplanet atmosphere spectra, we are starting to understand the chemical and physical processes taking place in these hot Jupiters. For example, statistical studies (Sing et al. 2016; Fu et al. 2017) have provided valuable insights into how aerosol presence varies in different atmospheric conditions and were later supported by detailed aerosol modeling (Gao et al. 2020). Comparative studies (Parmentier et al. 2018; Zhang et al. 2018; Garhart et al. 2020; Baxter et al. 2021; Wallack et al. 2021) have furthered our understanding of exoplanet thermal structures and heat circulation (Kataria et al. 2016). A large library of measured high quality high-precision exoplanetary spectra will be essential to our future studies of exoplanet atmospheres.

Here we present a uniformly analyzed transmission and emission spectrum of hot-Jupiter WASP-74b (Table 2) ranging from 0.3 to 4.5 μm using multiple instruments on the Hubble Space Telescope telescope (HST) and Spitzer Space Telescope (Spitzer). We have also compared our transit spectrum with previous ground-based observations and other independent analyses. We found a muted water absorption feature with a significant aerosol scattering slope in the transit spectrum, and a featureless blackbody-like WFC3/G141 eclipse spectrum with absorption feature in the Spitzer 3.6 μm bands.

2. Observations

We observed a total of six transits and three eclipses of WASP-74b using multiple instrument modes on HST and Spitzer (Table 1). The data comprises two observation programs and some parts of the data were published in previous studies (Mancini et al. 2019; Garhart et al. 2020; Luque et al. 2020). We have uniformly analyzed the full data set including new HST/STIS transit, HST/WFC3, and Spitzer eclipse. All the data are reduced using the same orbital parameters and limb-darkening coefficients from the same 3D stellar model.

3. Data Analysis

3.1. HST STIS Data Reduction

HST orbits around the earth every 90 minutes which results in an observing gap of ~ 45 minutes when the target is not in the continuous viewing zone. Combined with the thermal breathing of HST, this leads to an orbital-dependent systematics of the light



Table 1
A List of our Six Transit and Three Eclipse Observations of WASP-74b

WASP-74b Transit Observations					
	Grism/Filter	Visit 1	Visit 2	GO Program ID	PI
HST STIS	G430L	2017-05-04	2017-07-20	14767	Sing & López-Morales
HST STIS	G750L	2017-06-20		14767	Sing & López-Morales
HST WFC3	G141	2016-10-06		14767	Sing & López-Morales
Spitzer	IRAC 3.6	2017-01-14		13044	Deming
Spitzer	IRAC 4.5	2017-01-16		13044	Deming
WASP-74b Eclipse Observations					
	Grism/Filter	Visit 1	GO Program ID	PI	
HST WFC3	G141	2017-05-02	14767	Sing & López-Morales	
Spitzer	IRAC 3.6	2017-01-15	13044	Deming	
Spitzer	IRAC 4.5	2017-02-12	13044	Deming	

Table 2
Parameters from Mancini et al. (2019)

WASP-74b Parameters		
Equilibrium temperature	T_{eq} (K)	1926^{+21}_{-21}
Radius	R_p (R_{Jup})	$1.404^{+0.018}_{-0.012}$
Mass	M_p (M_{Jup})	$0.826^{+0.015}_{-0.014}$
Period	P_{orb} (days)	$2.1377445^{+0.0000018}_{-0.0000018}$
Semimajor axis	a (au)	$0.03443^{+0.00022}_{-0.00029}$
Inclination	i (degree)	$79.86^{+0.21}_{-0.21}$

curve. Various detrending techniques (Sing et al. 2011; Nikolov et al. 2014) have been developed to correct for this effect. Sing et al. (2019) used the time-tagged engineering information from the jitter files for each exposure to construct a parametric model. This new jitter decorrelation method was shown to improve the photometric performance of HST STIS time-series observations compared to previous used methods (Sing et al. 2019).

The STIS data reduction pipeline we used in this paper is identical to the jitter decorrelation method detailed in Sing et al. (2019), except it is applied on G430L and G750L data instead of the NUV-MAMA detector with E230M echelle grating. The orbital parameters (Table 2) have been fixed to the values used in Mancini et al. (2019). For limb darkening (Table 9), we used the 3D stellar model from the Stagger-grid (Magic et al. 2015) with the parameters $T_{\text{eff}} = 6000$ K, $\log g = 4$, $[\text{Fe}/\text{H}] = 0$. The systematics corrected light curves and residuals for two G430L visits and one G750L visit are shown in Figures 10–12.

3.2. HST WFC3 Data Reduction

The HST WFC3 data reduction pipeline is exactly the same as detailed in Fu et al. (2021) for both transit and eclipse. We used a combination of the BATMAN light-curve model (Kreidberg 2015) with the RECTE charge trapping systematics model (Zhou et al. 2017) for light-curve detrending. The orbital parameters (Table 2) have been fixed to the values used in Mancini et al. (2019) and the limb-darkening coefficients are from the same stellar model used for the STIS data reduction.

3.3. Spitzer Data Reduction

Two transits and eclipses of WASP-74b were observed with Spitzer’s InfraRed Array Camera (IRAC; Fazio et al. 2004), at

both 3.6 and 4.5 μm (PI: D. Deming, Program ID 13044). Table 1 includes the observation dates for these events. Each event used an exposure time of 0.4 s and covered approximately 7 hr total. For data reduction and analysis we use the Photometry for Orbits, Eclipses, and Transits pipeline (Campo et al. 2011; Stevenson et al. 2012; Cubillos et al. 2013).

Spitzer IRAC photometry has been the major instrument mode used to investigate exoplanet atmospheres in the infrared (Deming & Knutson 2020). The raw data is usually dominated by instrumental systematics due to intrapixel sensitivity variations on the detector in both 3.6 and 4.5 μm channels (Deming et al. 2015). During the past decade we have developed multiple methods (Deming et al. 2015; Stevenson et al. 2012) to mitigate this effect. Recently, May & Stevenson (2020) and May et al. (2021) generated a new Gaussian centroided intrapixel sensitivity map based on years of archival Spitzer calibration data. Here we use this fixed sensitivity map May & Stevenson (2020) to analyze the 4.5 μm Spitzer data sets while using standard BLISS mapping at 3.6 μm (Figure 2). At 3.6 μm we also find that the inclusion of a second-order function with respect to the widths derived from 2D Gaussian fits (PRF-FWHM) is optimal. Figure 1 shows the x- and y-pixel locations, and raw flux for all Spitzer IRAC data sets analyzed here.

For the astrophysical signal, we fit transits using the BATMAN (Kreidberg 2015) with limb-darkening coefficients fixed to values taken from the same stellar models as those used for the optical data reductions. Eclipses are modeled using the analytical model in Mandel & Agol (2002). All orbital parameters (Table 2) are fixed to the same values used in the HST STIS and WFC3 data reduction to minimize systematic offsets between the data sets.

At the beginning of the observation, instrument systematics are the strongest due to the time needed for the telescope pointing to stabilize and the detector to fill up the charge traps. Therefore, the resulting ramp effect at the beginning is challenging to model and the first portion of the data has usually been discarded (Stevenson et al. 2012; Garhart et al. 2020; Baxter et al. 2021). For this work, we have experimented varying the amount of data points to trim at the beginning of the observation from 0 to 120 minutes while fitting the remaining light curve with four different ramp models (Figure 3; left panels show transits and right panels show eclipses).

As expected, because the fixed sensitivity map is not dependent on other modeling choices like a standard BLISS map, its use at 4.5 μm results in minimal variations of the

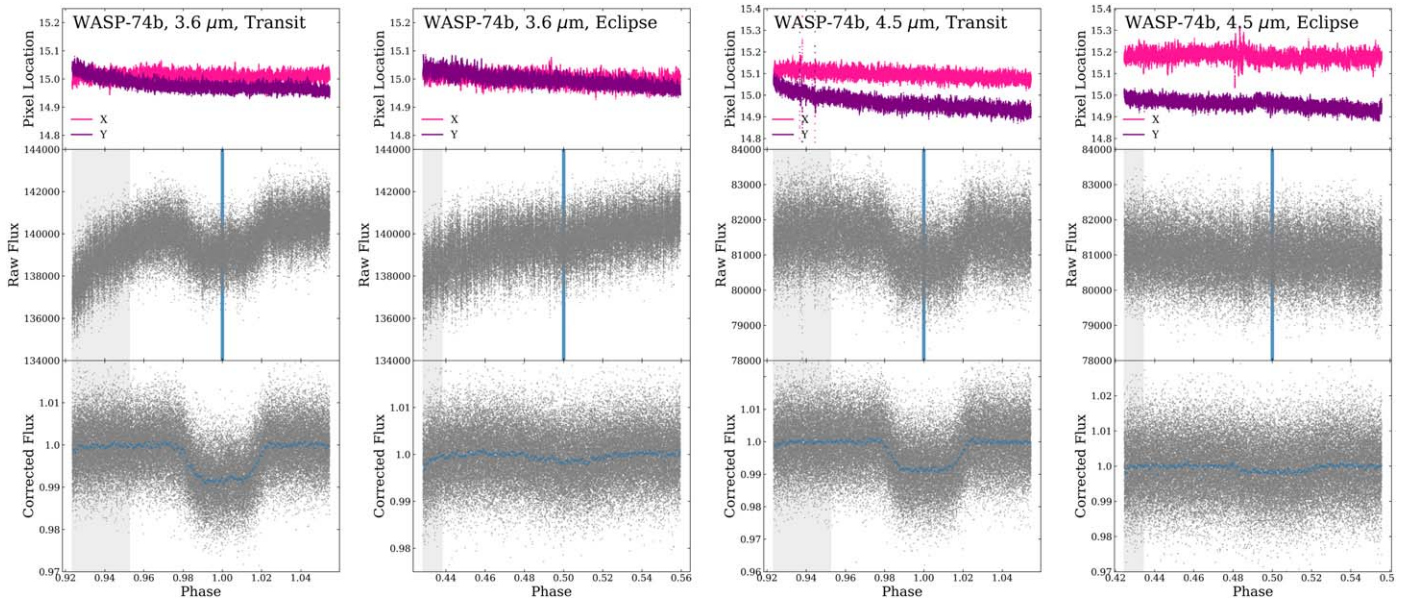


Figure 1. Centroids (top panels), raw flux (middle panels), and corrected flux (bottom panels) as a function of phase for all four Spitzer IRAC data sets as labeled. One can see that the 3.6 μm data sets are more heavily affected by a visit-long ramp, in combination with a stronger initial ramp for the 3.6 μm transit event. The trimmed parts of the light curves are shaded in gray.

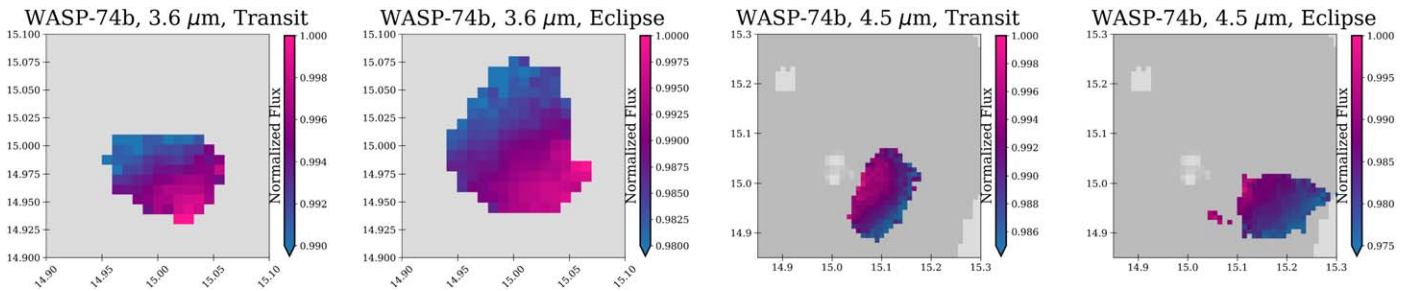


Figure 2. BLISS maps from best fits for all four Spitzer IRAC events as labeled. For the 4.5 μm maps, the darker gray regions denote where the fixed sensitivity map exists. Axis units are in subpixels. The BLISS map shown here is the subset of the fixed sensitivity map at the locations of the data centroids. It is not generated from this 4.5 micron data set.

measured eclipse and transit depths with the amount of data trimmed from the beginning (bottom two panels of Figure 3), while the free BLISS map used for 3.6 μm results in transit and eclipse depths which are heavily dependent on the amount of data trimmed and ramp model used. In Figure 3 we also denote the ramp that has the lowest Bayesian information criterion at each trim level with a black circle around the data point. This further demonstrates that the 4.5 μm data sets are no longer beholden to the whims of the systematic removal with the best-fit ramp the same across all trim levels, while the 3.6 μm events best-fit ramp depends on the trim level. To address this, we select trimming that results in all ramps measuring the approximately the same depths based on the 3.6 μm events, and adopt the same trimming at 4.5 μm for consistency. We select 90 minutes of trimming for the transits, and 30 minutes of trimming for the eclipses.

Our final fits use a linear ramp and 2nd order PRF-FWHM and standard BLISS map detrending at 3.6 μm with a 90 minute trim for the transit and a 30 minute trim for the eclipse. Our 4.5 μm fits use a linear ramp and fixed sensitivity map detrending for both events, with the same trimming as 3.6 μm .

4. Simultaneous Ground-based Photometric Monitoring

To search for the presence of magnetic activity in WASP-74, we performed nightly photometry on the star during the

2018–2021 observing seasons with the Tennessee State University Celestron 14 inch (C14) automated imaging telescope (AIT) located at Fairborn Observatory in southern Arizona (e.g., Henry et al. 2000; Oswalt 2003). The AIT is equipped with an SBIG STL-1001E CCD camera and uses a Cousins R filter. Each observation consists of 3–5 consecutive exposures on WASP-74 and several surrounding comparison stars in the same CCD field of view. The individual frames are coadded and reduced to differential magnitudes in the sense WASP-74 minus the mean brightness of the comparison stars. Further details of our observing, reduction, and analysis techniques can be found in Sing et al. (2015).

A total of 245 good nightly observations were collected between 2018 March 4 and 2021 June 18 (plus a few transit observations that we discarded). The observations are summarized in Table 3. The standard deviation of the individual nightly observations from the mean of the complete data set is 0.00262 mag, which is close to the typical precision of a single observation with the C14. The seasonal means agree to within 0.0007 mag. Thus, we confirm the findings of Hellier et al. (2015) that WASP-74 is magnetically inactive and photometrically constant.

The photometric observations are plotted in the top panel of Figure 4 where the vertical dotted lines mark the beginning of

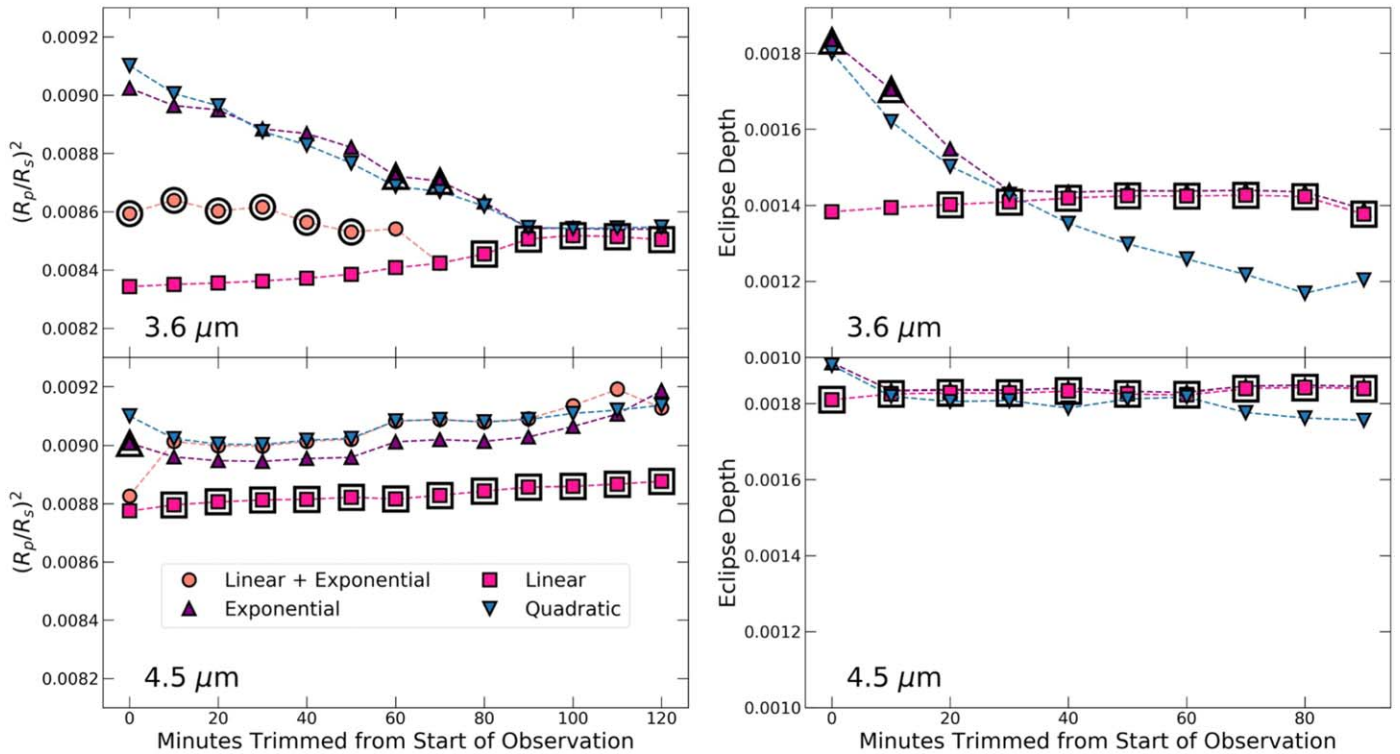


Figure 3. Demonstration of the dependence on ramp choice and amount of data trimmed from the start of events. The 3.6 and 4.5 μm events are shown on the same scale for ease of comparison. Left: transits. Right: eclipses. Top: 3.6 μm . Bottom: 4.5 μm . Our use of the fixed sensitivity map for systematic removal at 4.5 μm results in a consistent eclipse and transit depth regardless of pretrimming and ramp model, while the 3.6 μm events are heavily dependent on the choice of these parameters due to the flexibility of the BLISS map.

Table 3
Summary of C14 ait Photometry of Wasp-74

Observing Season	N_{obs}	Date Range (HJD - 2,400,000)	Sigma (mag)	Seasonal Mean (mag)
(1)	(2)	(3)	(4)	(5)
2018	119	58182–58477	0.00242	-2.32081
2019	69	58572–58832	0.00243	-2.32147
2020	28	58925–59182	0.00338	-2.32104
2021	29	59281–59383	0.00302	-2.32146

each calendar year. WASP-74 comes to opposition in late July; this means we lose the central part of each seasonal light curve because we must shut down our telescopes during the summer “monsoons” of southern Arizona (typically early July to early September). The summer gap is visible in the 2018, 2019, and 2020 observing seasons, but not in 2021 since the latest observations end at the shutdown. A frequency spectrum, based on least-squares fitting of sine curves, is shown in the bottom panel of Figure 4. No significant periodicity is seen in the range 1–100 days. Separate analyses of the individual observing seasons similarly showed no significant periodicities.

We phased the nightly observations to the radial-velocity period and computed a new least-squares sine fit. The formal peak-to-peak amplitude of the photometry is 0.00093 ± 0.00047 , consistent with zero to better than one mmag. This confirms that radial-velocity variations in WASP-74 are indeed due to planetary reflex motion and not line-profile variations due to spots (e.g., Queloz et al. 2001; Paulson et al. 2004).

We did not detect any strong stellar variability with our three-years ground-based photometric monitoring campaign.

Therefore any offsets in transit and eclipse depth between different observations are unlikely to be caused by changing in host star brightness from stellar activities such as varying starspots coverage.

5. Comparison with Previous Studies

We have compared our transmission spectrum (Table 8) with previous studies from Luque et al. (2020) and Mancini et al. (2019), which include multiple ground-based photometric points with WFC3 G141 and Spitzer data sets (Figure 5). System parameters (Table 2) used in data reduction for this work were fixed to the same exact values used in Mancini et al. (2019) to avoid any offsets from light-curve fitting.

Our STIS spectrum sits between the ground-based photometry points in transit depth reported in Mancini et al. (2019) and Luque et al. (2020). The tension between STIS and ground-based results could come from the different treatments used in reducing noisy ground-based light curves detailed in Luque et al. (2020). We find no evidence supporting neither strong TiO/VO absorption indicated by increased transit depth in the optical ($\sim 500\text{--}700\text{ nm}$; Mancini et al. 2019) nor super-Rayleigh scattering (Luque et al. 2020).

The reduced WFC3 G141 transit spectrum has a large offset compared to Mancini et al. (2019). Luque et al. (2020) took the exact same WFC3 G141 spectrum from Mancini et al. (2019) and added an offset parameter in their PLATON retrieval. Our WFC3 G141 spectrum is highly consistent with the WFC3 offset version 2 reported in Luque et al. (2020). Kevin Stevenson (KS hereafter) also performed an independent analysis for the WFC3 G141 spectrum (Figure 5) with procedures detailed in Stevenson & Fowler (2019), Stevenson et al. (2014) using the same exact

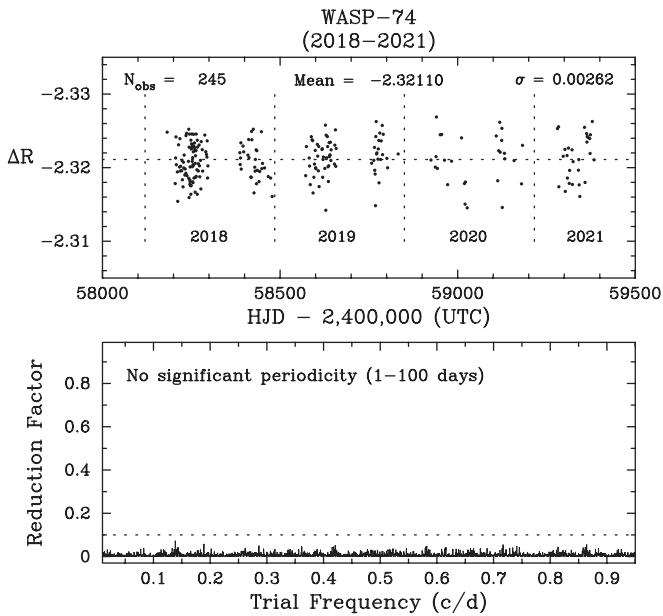


Figure 4. Top: the Cousins R -band photometry of WASP-74 from 2018–2021, acquired with the C14 AIT at Fairborn Observatory. The star is constant on night-to-night and year-to-year timescales to the limit of our precision. Bottom: frequency spectrum of the complete data set shows no significant periodicity between 1 and 100 days. The horizontal dashed line in the bottom panel represents the noise limit below which reliable periods are not found in multicolor photometry (Henry et al. 2011).

orbital parameters used in (Mancini et al. 2019) and this work. The independently analyzed WFC3 G141 spectrum from KS is consistent with this work and WFC3 offset 2 version from Luque et al. (2020) and also has a large offset compared to Mancini et al. (2019).

Our Spitzer points are lower than reported in Luque et al. (2020) with channel 1 ($\sim 3\sigma$ lower) having a larger offset than channel 2 ($\sim 2\sigma$ lower). This could be due to the different choices of the minutes of data trimmed at the start of the observation and the ramp models. As shown in Figure 3, we have extensively explored the different combinations of minutes to trim and ramp models. Our Spitzer spectrum represents transit depths from the best fitted light curves.

We also compared our Spitzer eclipse spectrum with Garhart et al. (2020). While the $3.6\ \mu\text{m}$ point is in agreement, our $4.5\ \mu\text{m}$ point is lower by $\sim 2.5\sigma$ (Figure 6). Garhart et al. (2020) used orbital parameters from the discovery paper (Hellier et al. 2015) and we used the ones from Mancini et al. (2019) to be consistent with the rest of this study.

6. PLATON Retrieval

6.1. Transit Retrieval

We performed a retrieval analysis with PLATON (Zhang et al. 2020) on both uniformly analyzed transit (Table 8) and eclipse (Table 10) spectra of WASP-74b. All retrievals were conducted with opacity sampling at $R = 1000$ and 1000 live points. Our setup for the transit retrieval is shown in Table 4 with seven free parameters assuming equilibrium chemistry and including condensation. The best-fit PLATON retrieval model with a χ^2_ν of 1.59 is shown in Figure 7. The model shows a very muted $1.4\ \mu\text{m}$ water feature accompanied with a strong scattering slope extending from the optical to infrared.

We found the metallicity and C/O ratio consistent with solar values (Figure 15). The retrieved limb averaged temperature from the transit spectrum based on 1D models is typically lower compared to the equilibrium temperature in hot Jupiters. This is because atmospheric circulation causes an always colder western limb to the eastern limb (Showman et al. 2009) and 1D models retrieve a single uniform temperature for both limbs that could be biased toward lower temperature by several hundred degrees (MacDonald et al. 2020). In the colder western limb, aluminum- and silicate-based aerosols can form under these cooler environments which lead to strong scattering effect and muted molecular absorption features (Muñoz & Isaak 2015; Parmentier et al. 2016).

We also performed a retrieval using the same priors but without the $3.6\ \mu\text{m}$ Spitzer point (Figure 7). The Spitzer channel 1 transit depth can vary by several hundred ppm based on the trimming choice at the beginning of the light curve (Figure 3). Excluding the $3.6\ \mu\text{m}$ point allows us to investigate if our retrieval result hinges on this one data point. The low transit depth of the $3.6\ \mu\text{m}$ point does drive up the retrieved log-scattering factor (Tables 4 & 5) from $3.79^{+1.68}_{-1.32}$ to $6.68^{+1.50}_{-1.89}$ as expected since a stronger scattering is needed to fit for the steeper slope. However, all other retrieved parameters stay consistent with or without the $3.6\ \mu\text{m}$ point.

6.2. Eclipse Retrieval

For the eclipse retrieval (Figure 8) we also assumed equilibrium chemistry with a total of six free parameters (Table 6) including three TP-profile parameters (Line et al. 2013). The T_{int} is set to 100K. The best-fit model with a χ^2_ν of 1.47 is shown in Figure 8 and the TP profile is shown in Figure 9 with dash lines indicating one sigma uncertainty. The WFC3/G141 emission spectrum is very close to blackbody-like with a potentially weak water absorption feature. The Spitzer $3.6\ \mu\text{m}$ point is $\sim 3\sigma$ lower than a blackbody of 2260K assuming dayside heat redistribution which indicates a possible molecular absorption features. The strongest opacity source covered by the $3.6\ \mu\text{m}$ band is CH_4 . Although large quantities of methane are unlikely to exist under a dayside temperature $> 2000\ \text{K}$, some amount could be present in the higher altitude and cooler environment combined with a high C/O ratio atmosphere (Moses et al. 2013).

The emission spectrum probes deeper into the atmosphere at around 1–5 bar and the retrieved decreasing TP profile at those pressure levels is consistent within one sigma compared to what we expect from dayside heat redistribution (2260K) on WASP-74b. The retrieved high C/O ratio of 1.31 is surprising since it would indicate very low water abundance with high-abundance carbon-bearing species such as CO and CH_4 . We believe this high C/O ratio is driven by the featureless G141 spectrum combined with the low Spitzer $3.6\ \mu\text{m}$ point. This combination led to a low water-abundance solution that suppresses the water absorption feature one would expect in a decreasing TP profile while maintaining the methane absorption feature in the Spitzer channel 1 band.

We believe three potential causes could have explained this unusually high C/O ratio indicated by the emission spectrum. One would be the reliability of Spitzer $3.6\ \mu\text{m}$ point, which has been shown to be challenging to analyze due to the more complex instrument systematics compared to the $4.5\ \mu\text{m}$ channel (May & Stevenson 2020). A higher $3.6\ \mu\text{m}$ point with no methane absorption feature would indicate a more

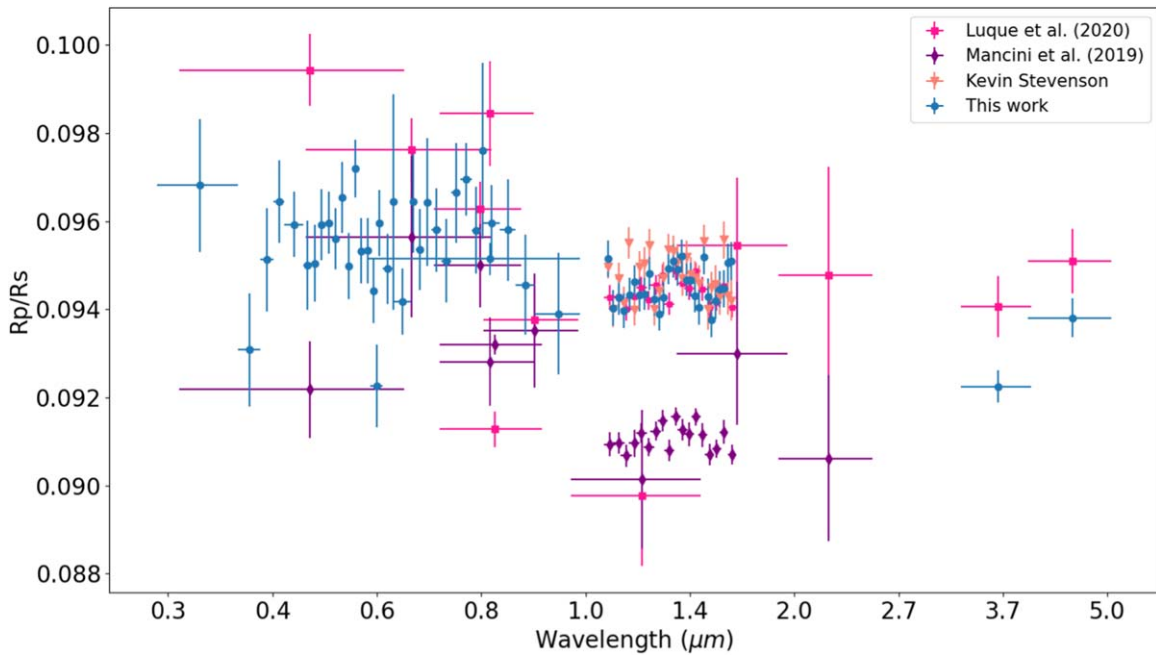


Figure 5. Comparison of transit spectra from this study to previous studies. We have fixed all orbital parameters to the exactly values as used in (Mancini et al. 2019).

Table 4

PLATON Transit Retrieval Results (Full Spectrum)

Parameter	Priors	Posteriors	Best Fit
T	$\mathcal{U}(950, 1900)$	1288^{+282}_{-228}	1557
$R_{pl}(\text{Jup})$	$\mathcal{U}(1.1232, 1.404)$	$1.33^{+0.02}_{-0.03}$	1.34
$\log f_{\text{scatter}}$	$\mathcal{U}(0, 10)$	$6.68^{+1.50}_{-1.39}$	3.97
$\log(Z/Z_{\odot})$	$\mathcal{U}(-1, 1)$	$0.03^{+0.61}_{-0.65}$	-0.37
C/O ratio	$\mathcal{U}(0.05, 2)$	$0.85^{+0.72}_{-0.51}$	0.19
$\log P_{\text{cloudtop}} (\text{Pa})$	$\mathcal{U}(0, 8)$	$4.29^{+2.39}_{-2.39}$	7.08
error multiple	$\mathcal{U}(0.5, 5)$	$1.25^{+0.11}_{-0.10}$	1.23
scatter slope	$\mathcal{U}(0, 10)$	$2.81^{+0.94}_{-0.78}$	2.27

Table 5

PLATON Transit Retrieval Results (Without the 3.6 μm Point)

Parameter	Priors	Posteriors	Best Fit
T	$\mathcal{U}(950, 1900)$	1413^{+333}_{-276}	1458
$R_{pl}(\text{Jup})$	$\mathcal{U}(1.1232, 1.404)$	$1.35^{+0.02}_{-0.05}$	1.37
$\log f_{\text{scatter}}$	$\mathcal{U}(0, 10)$	$3.79^{+1.68}_{-1.32}$	2.82
$\log(Z/Z_{\odot})$	$\mathcal{U}(-1, 1)$	$-0.08^{+0.66}_{-0.59}$	-0.21
C/O ratio	$\mathcal{U}(0.05, 2)$	$0.67^{+0.76}_{-0.40}$	0.81
$\log P_{\text{cloudtop}} (\text{Pa})$	$\mathcal{U}(0, 8)$	$4.33^{+2.27}_{-2.44}$	7.41
error multiple	$\mathcal{U}(0.5, 5)$	$1.15^{+0.11}_{-0.09}$	1.07
scatter slope	$\mathcal{U}(0, 10)$	$2.23^{+1.33}_{-0.90}$	1.56

isothermal TP profile which would not need an extremely low water abundance to fit the featureless G141 spectrum. Another cause could be the present of an unknown opacity source in the G141 band masking out the water absorption feature. We know H- can have this effect (Lothringer et al. 2018; Parmentier et al. 2018; Arcangeli et al. 2019), but it only exists in ultrahot Jupiters (>2500K) and WASP-74b is not hot enough for H- to become a dominate opacity source. We ran the retrievals with H- turned on and off and there were no changes in the retrieval results. High C/O ratio could also be due to planet formation

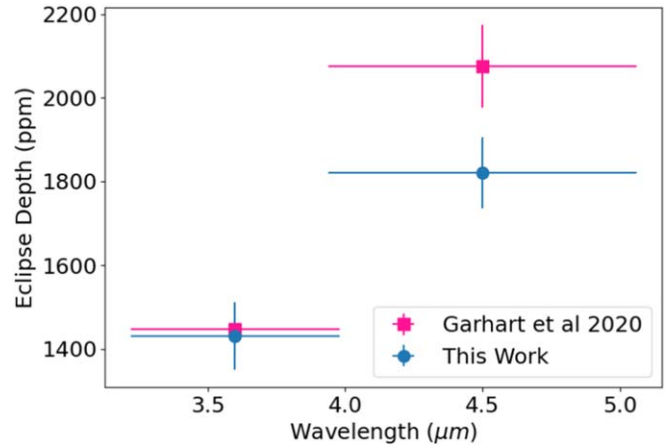


Figure 6. Comparison of Spitzer eclipse spectra from this study to Garhart et al. (2020). We have fixed all orbital parameters to the exactly values as used in Mancini et al. (2019).

beyond the snowline where the oxygen was locked up in the water ice while carbon was still free as CO in the gaseous phase (Öberg et al. 2011; Madhusudhan 2012).

We also performed a retrieval on the emission spectrum without the 3.6 μm point to see how much this one data point affects the retrieval result. The C/O ratio drops significantly (Tables 6 and 7) from $1.31^{+0.41}_{-0.26}$ to $0.92^{+0.30}_{-0.06}$ showing the low 3.6 μm point is driving up the methane abundance and thus the C/O ratio. All other parameters and the TP profile stayed consistent.

7. Follow-up Observations with JWST

The surprisingly high C/O ratio retrieval from the eclipse spectrum calls for JWST follow-up observations with extended wavelength coverage. Eclipse observations with NIRSpec G235 and G395 would cover multiple infrared features from CH₄, H₂O CO, and CO₂, which would allow us to precisely constrain the C/O ratio. For the transit spectrum, NIRISS SOSS will be able to confirm the strong scattering slope which

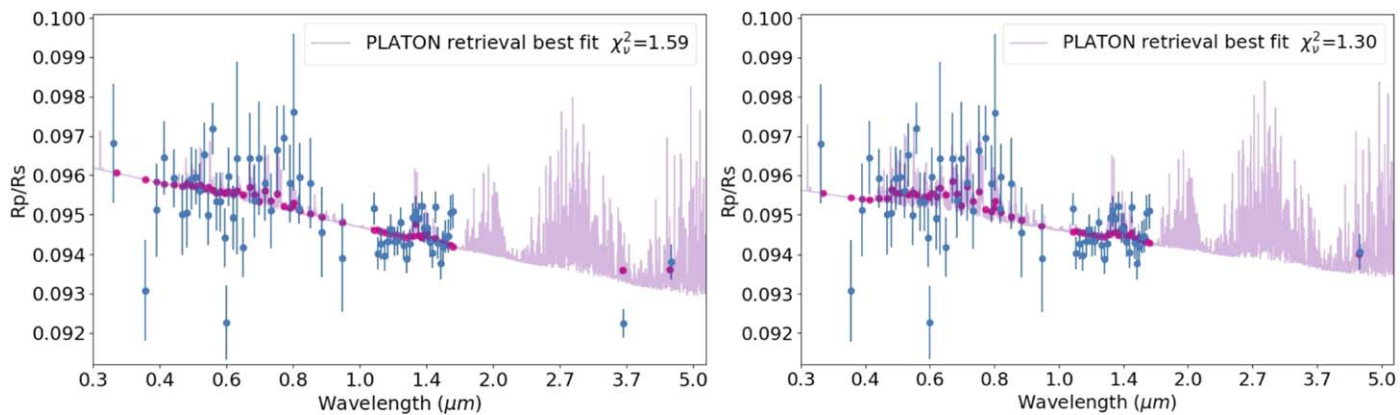


Figure 7. Best-fit PLATON retrieval of WASP-74b transit spectrum. The purple line is the full-resolution model with pink dots for corresponding binned model. The left panel uses the full spectrum and the right panel excludes the 3.6 μm point. We see strong scattering with muted water feature and no evidence for TiO absorption or super-Rayleigh scattering in both retrievals. However, the low 3.6 μm point does drive up the cloud scattering factor.

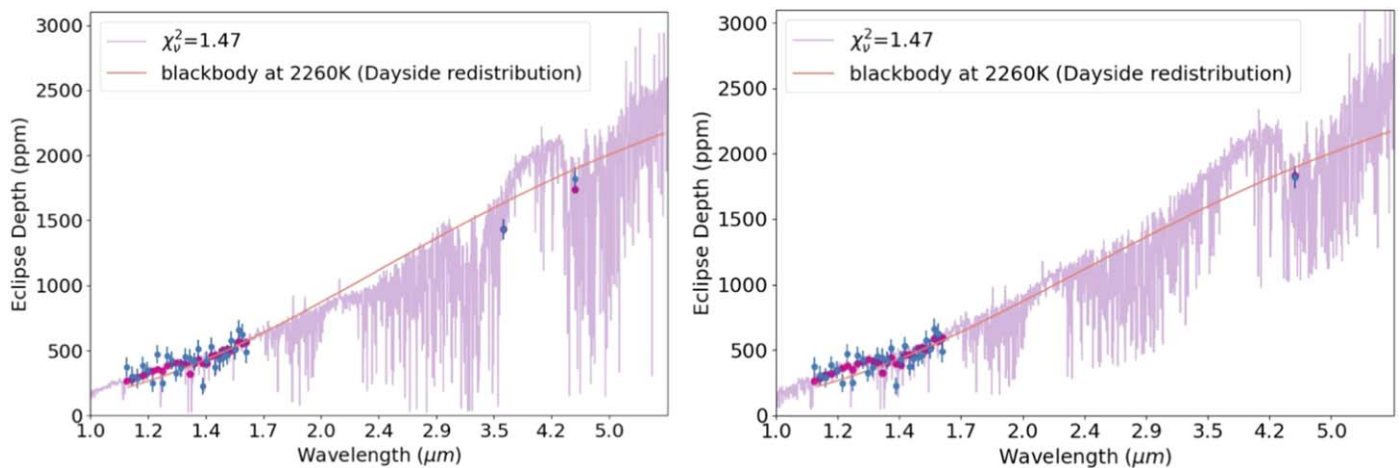


Figure 8. Best-fit PLATON retrieval of WASP-74b eclipse spectrum. The left panel uses the full spectrum and the right panel excludes the 3.6 μm point. The purple line is the full-resolution model with pink dots for corresponding binned model and overplotted with blackbody at 2260K in orange represent dayside only heat redistribution. In the full spectrum (left), we see a featureless blackbody-like WFC3/G141 spectrum with a methane absorption feature at 3.6 μm band. Without the 3.6 μm point (right), the methane absorption feature disappears and the retrieved C/O ratio drops significantly.

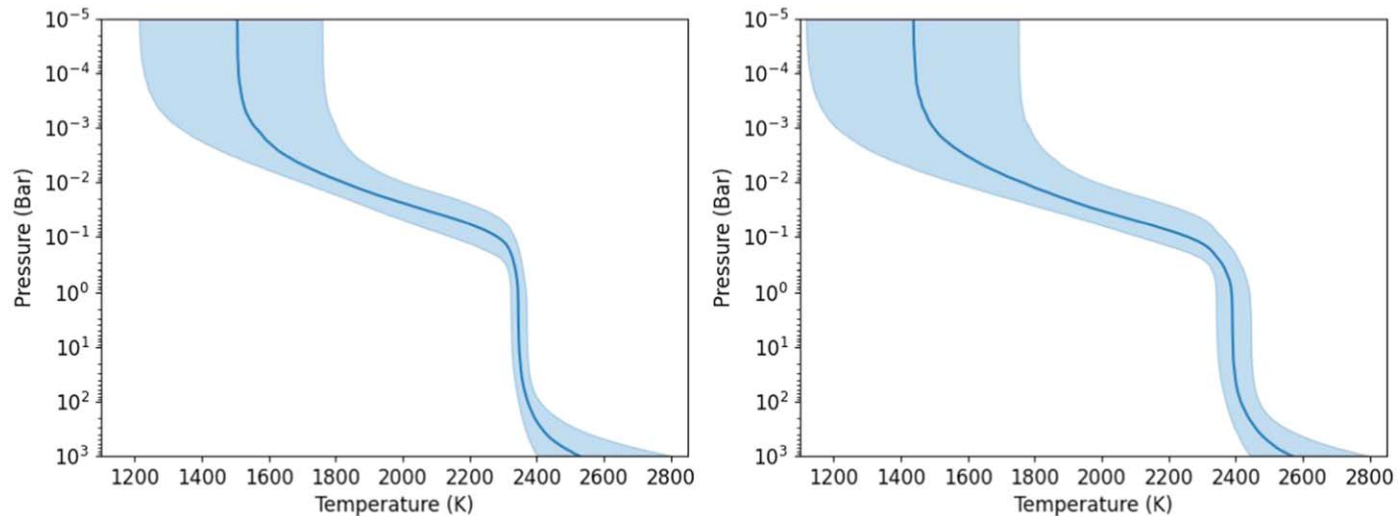


Figure 9. TP profile from PLATON eclipse retrieval with the solid line as the median values and shaded regions representing one sigma uncertainty. The left panel uses the full spectrum and the right panel excludes the 3.6 μm point. The TP profiles are highly consistent showing the thermal structure is not sensitive to the one 3.6 μm point.

Table 6
PLATON Eclipse Retrieval Results (Full Spectrum)

Parameter	Priors	Posteriors	Best Fit
$\log f_{\text{scatter}}$	$\mathcal{U}(0, 3)$	$1.0^{+0.79}_{-0.64}$	1.16
$\log(Z/Z_{\odot})$	$\mathcal{U}(-1, 3)$	$-0.30^{+0.66}_{-0.46}$	-0.76
C/O ratio	$\mathcal{U}(0.1, 2)$	$1.31^{+0.41}_{-0.26}$	0.90
β	$\mathcal{U}(0, 1.25)$	$0.88^{+0.13}_{-0.16}$	0.46
$\log \kappa_{\text{IR}}$	$\mathcal{U}(-4, -0.5)$	$-1.80^{+0.44}_{-0.68}$	-1.20
$\log \gamma$	$\mathcal{U}(-3, 0.5)$	$-0.80^{+0.28}_{-0.37}$	-2.01

extends from the optical into the infrared and better characterize the aerosol properties.

WASP-74b sits in an interesting transition parameter space between hot Jupiters and ultrahot Jupiters, where molecular features are not yet fully diminished by thermal dissociation and continuum opacity sources like H-, but high altitude aerosols can still linger to flatten the spectrum. Follow-up studies of WASP-74b with JWST will better our understanding of hot-Jupiter atmospheres in general and how the atmospheres change as they transition into ultra-hot-Jupiter atmospheres.

8. Conclusion

We observed six transits and three eclipses of the hot-Jupiter WASP-74b with HST STIS/WFC3 and Spitzer. All data sets were uniformly analyzed with the same orbital parameters and limb-darkening coefficients to ensure the consistence between different instruments. We have compared our transit spectrum with previous studies and we found no evidence for neither strong TiO/VO absorption in the optical as reported in Mancini et al. (2019) nor the super-Rayleigh scattering slope from Luque et al. (2020). Instead we found a muted water feature with strong aerosol scattering extending from the optical into

Table 7
PLATON Eclipse Retrieval Results (Without the 3.6 μm Point)

Parameter	Priors	Posteriors	Best Fit
$\log f_{\text{scatter}}$	$\mathcal{U}(0, 3)$	$1.03^{+0.74}_{-0.62}$	0.86
$\log(Z/Z_{\odot})$	$\mathcal{U}(-1, 3)$	$-0.28^{+0.86}_{-0.49}$	0.03
C/O ratio	$\mathcal{U}(0.1, 2)$	$0.92^{+0.30}_{-0.06}$	0.92
β	$\mathcal{U}(0, 1.25)$	$0.86^{+0.16}_{-0.18}$	0.87
$\log \kappa_{\text{IR}}$	$\mathcal{U}(-4, -0.5)$	$-1.86^{+0.45}_{-0.70}$	-2.09
$\log \gamma$	$\mathcal{U}(-3, 0.5)$	$-0.88^{+0.33}_{-0.43}$	-0.86

the infrared. Both metallicity and C/O ratio are consistent to the solar values within one sigma.

The eclipse retrieval results were more surprising with the preferred high C/O driven by possible CH₄ absorption feature in the Spitzer 3.6 μm band. However, this result is highly sensitive to a single Spitzer data point and future JWST follow-up observations are needed for further investigations.

Appendix

The appendix includes the reduced light curves with final spectrum and PLATON retrieval posteriors for both transmission and eclipse observations. For the transmission, we have two visits of STIS G430L (Figures 10, 11), one visit of STIS G750L (Figure 12), and WFC3 G141 (Figure 13). The final transmission spectrum and limb-darkening coefficients are listed in Tables 8 and 9. For the eclipse, we have one visit of WFC3 G141 (Figure 14). The final eclipse spectrum is listed in Table 10. The PLATON retrieval posteriors for transmission spectra with and without the Spitzer 3.6 μm point are shown in Figures 15 and 16. The PLATON retrieval posteriors for eclipse spectra with and without the Spitzer 3.6 μm point are shown in Figures 17 and 18.

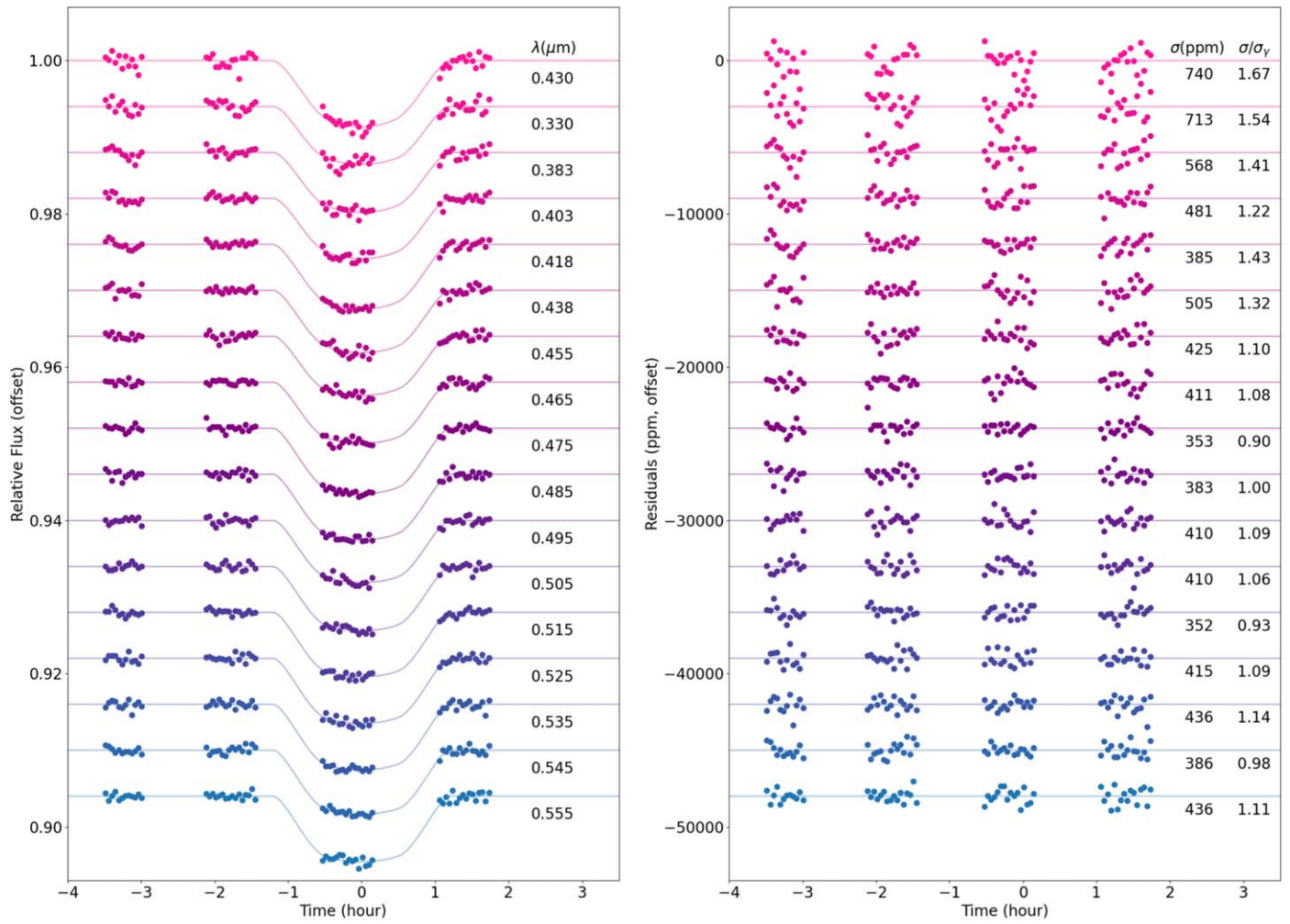


Figure 10. HST STIS G430L visit 1 spectral bin transit light curves after systematics correction using jitter decorrelation (left) and corresponding residuals (right).

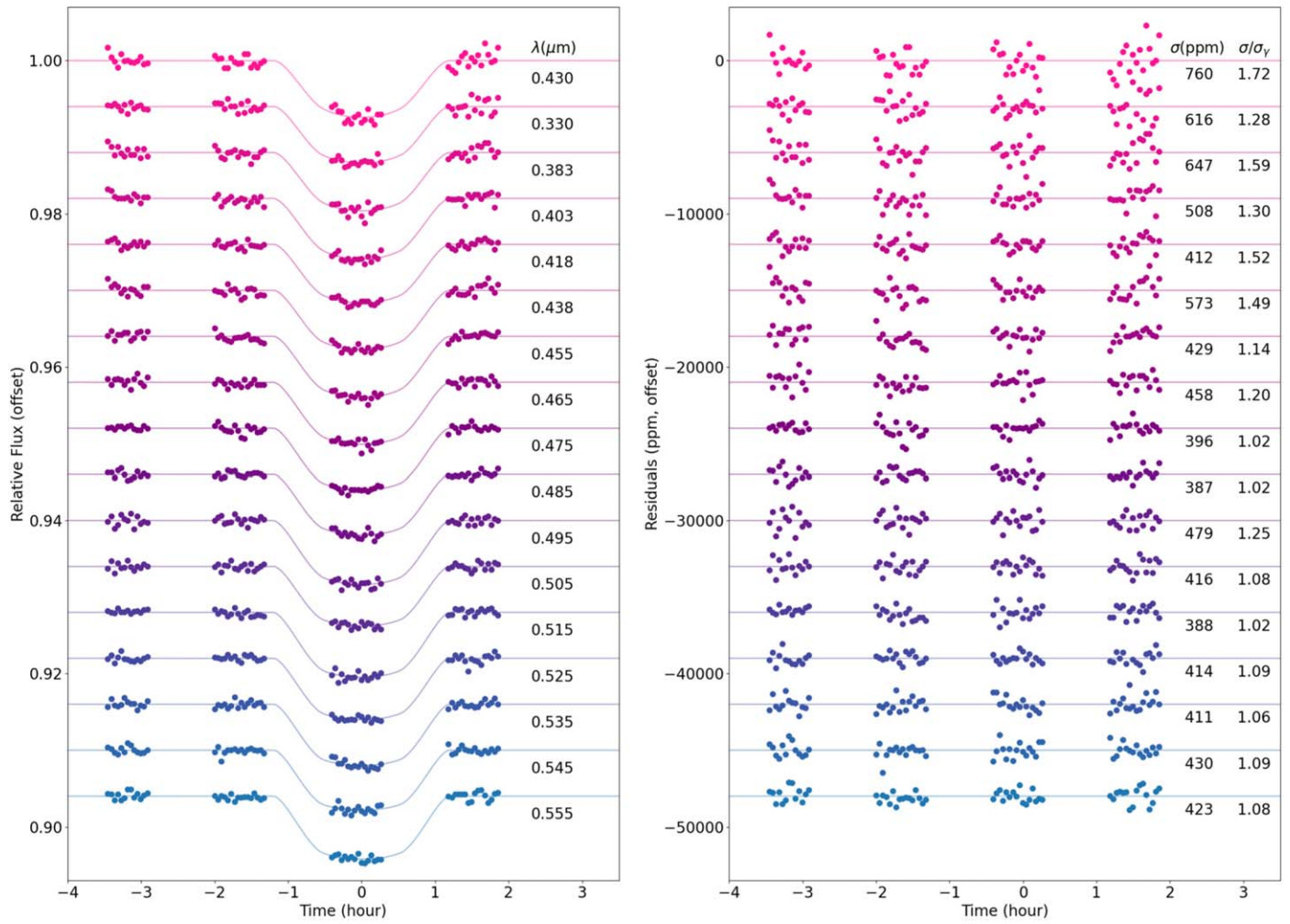


Figure 11. HST STIS G430L visit 2 spectral bin transit light curves after systematics correction using jitter decorrelation (left) and corresponding residuals (right).

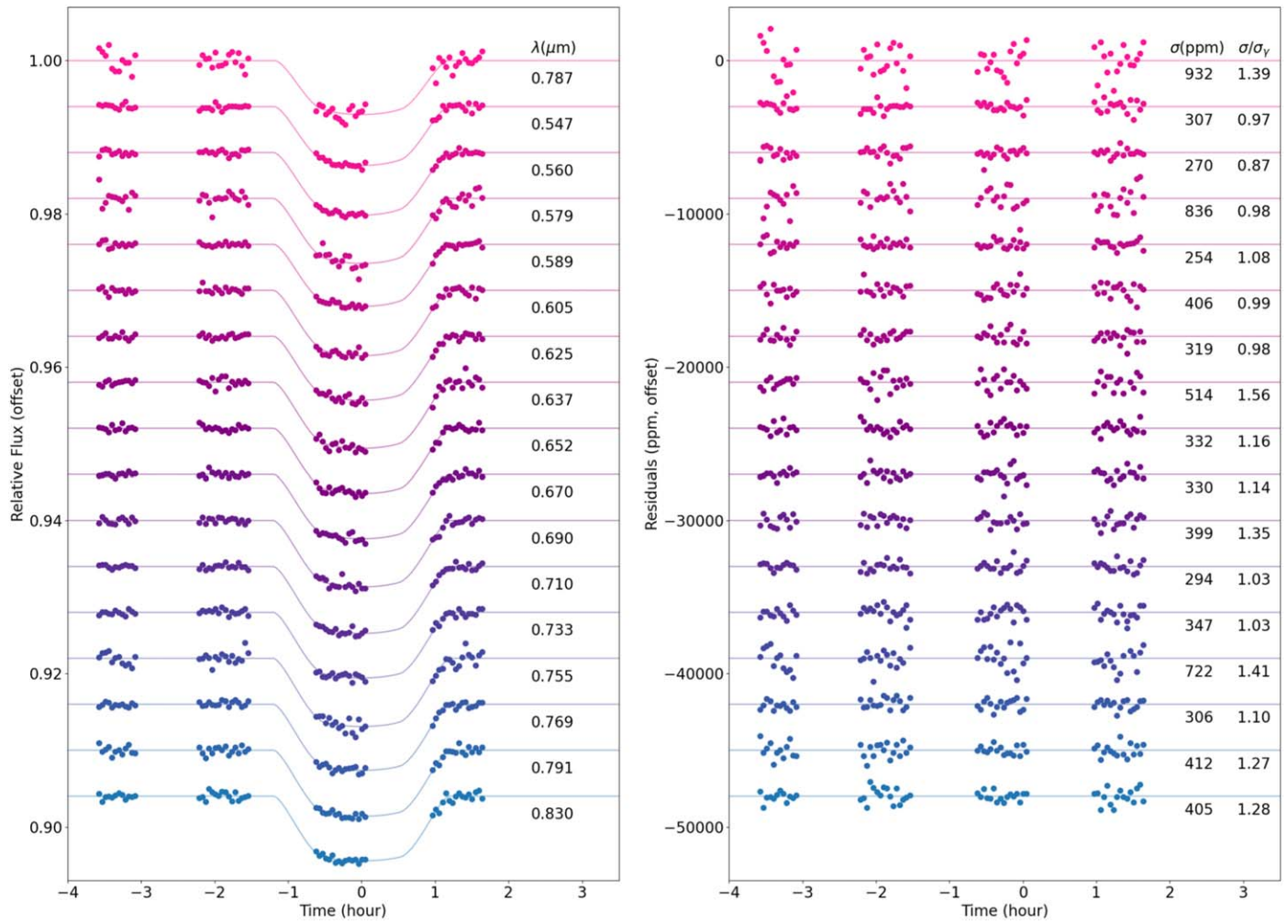


Figure 12. HST STIS G750L spectral bin transit light curves after systematics correction using jitter decorrelation (left) and corresponding residuals (right).

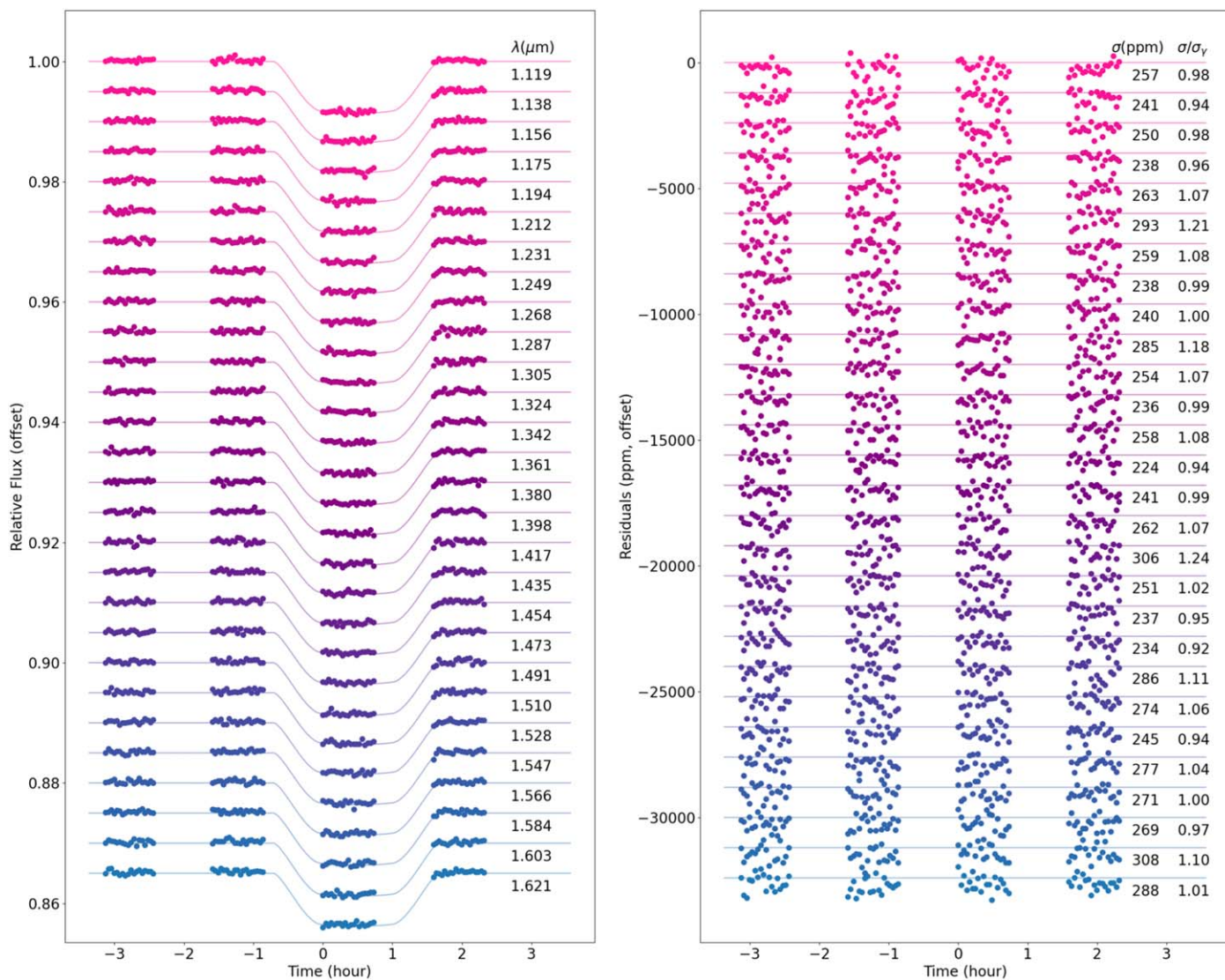


Figure 13. HST WFC3 G141 spectral bin transit light curves after ramp-effect correction using RECTE (left) and corresponding residuals (right).

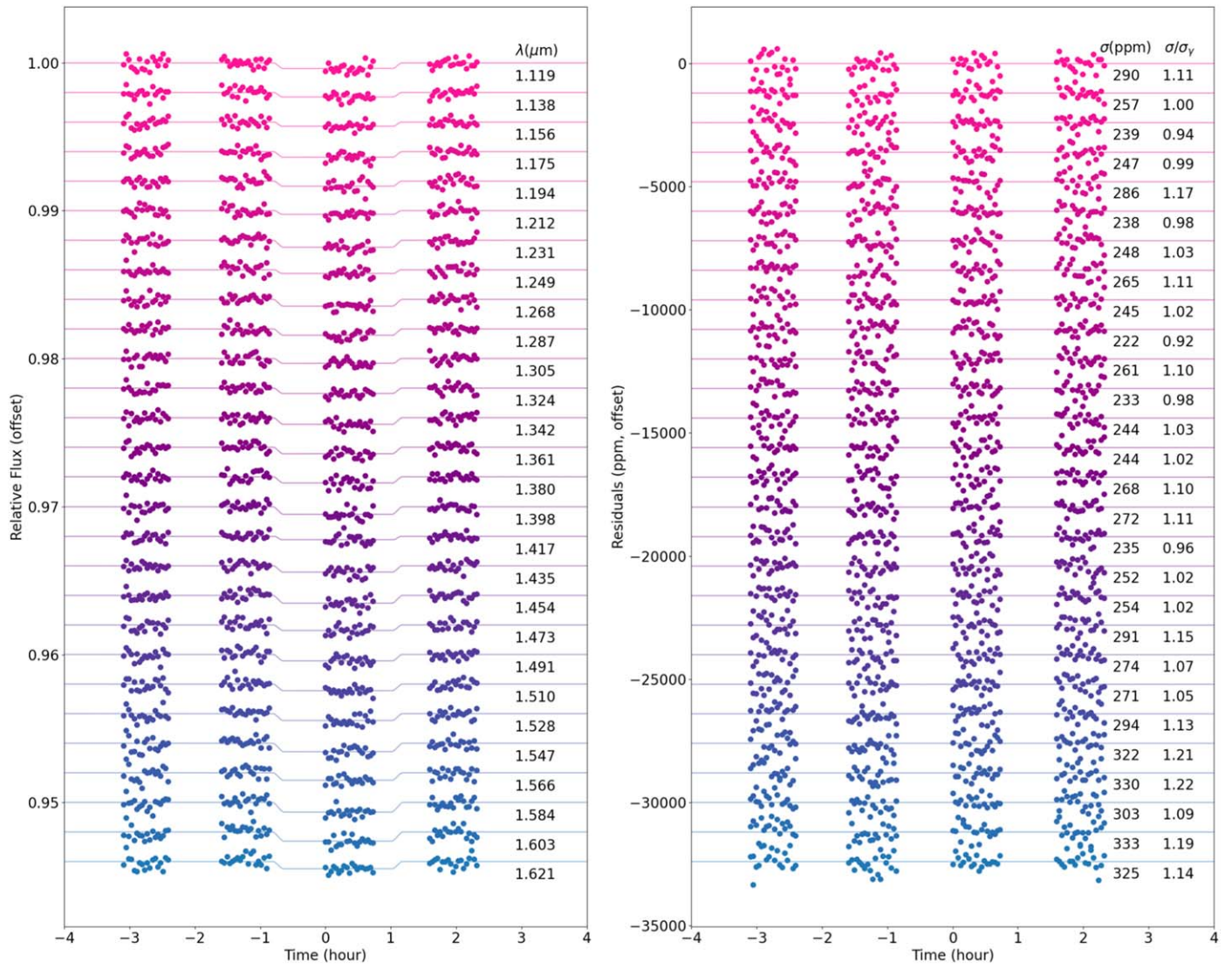


Figure 14. HST WFC3 G141 spectral bin eclipse light curves after ramp-effect correction using RECTE (left) and corresponding residuals (right).

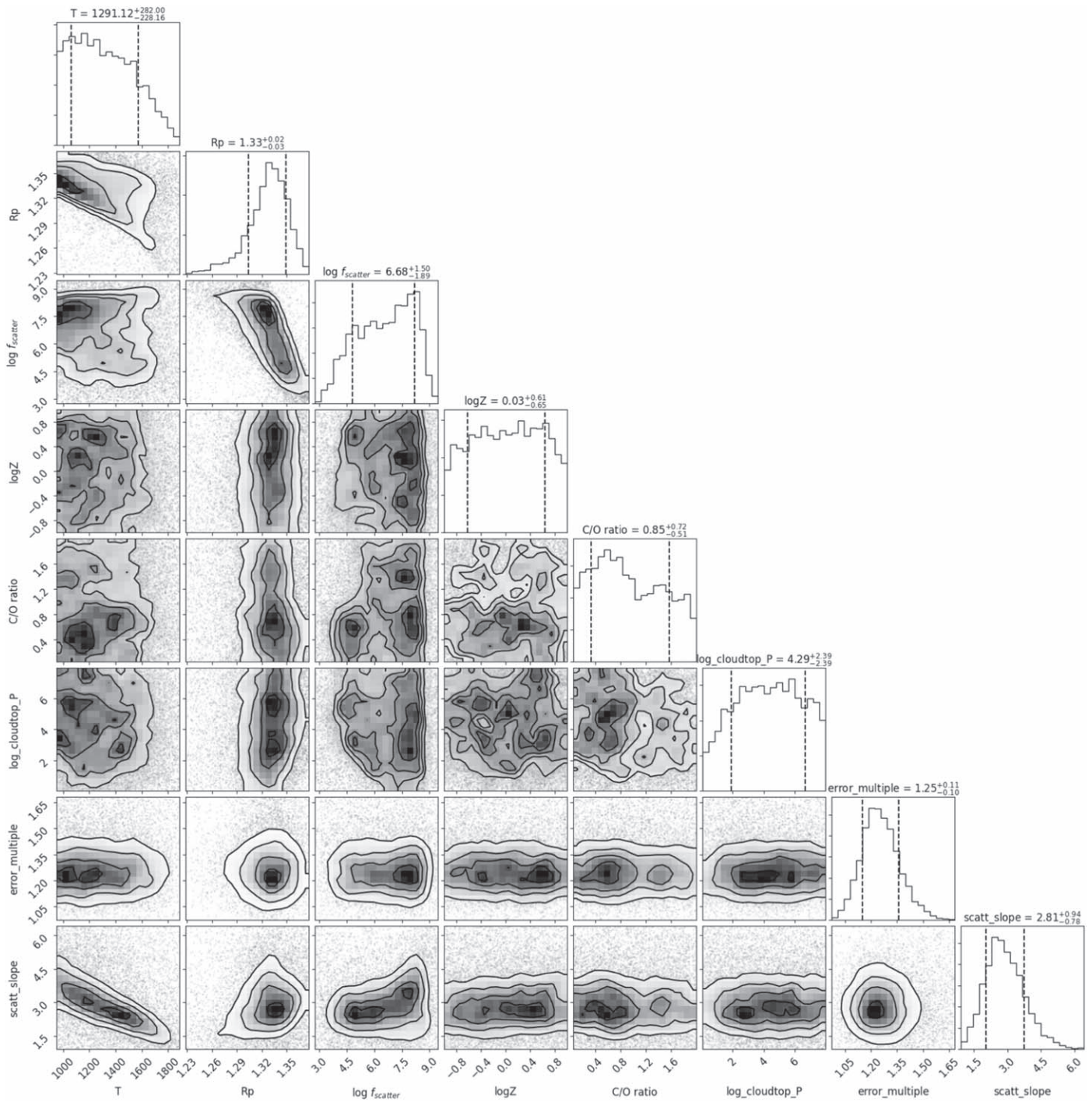


Figure 15. Posterior distribution of PLATON retrieval on the transit spectrum.

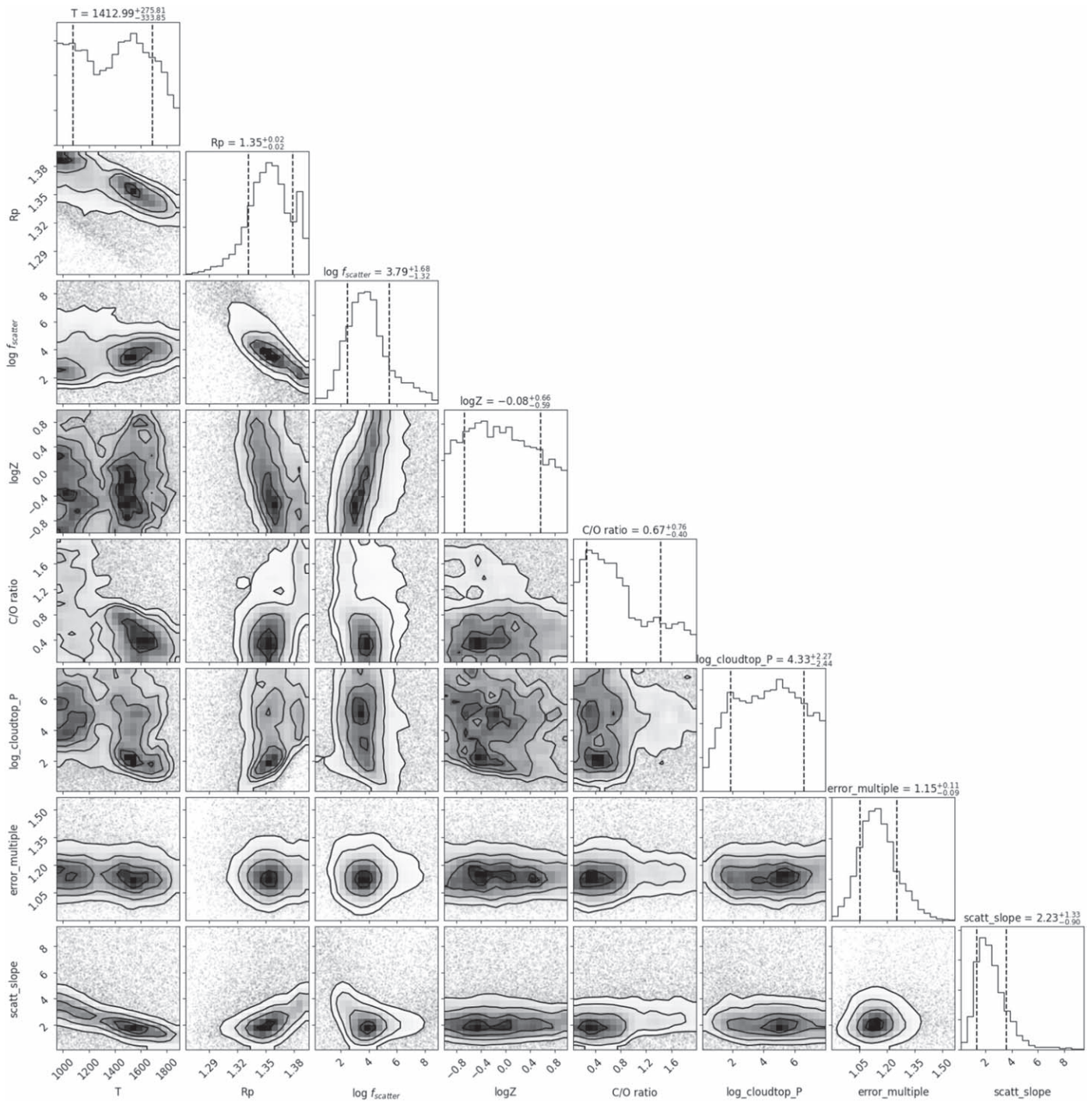


Figure 16. Posterior distribution of PLATON retrieval on the transit spectrum without the Spitzer $3.6 \mu\text{m}$ point.

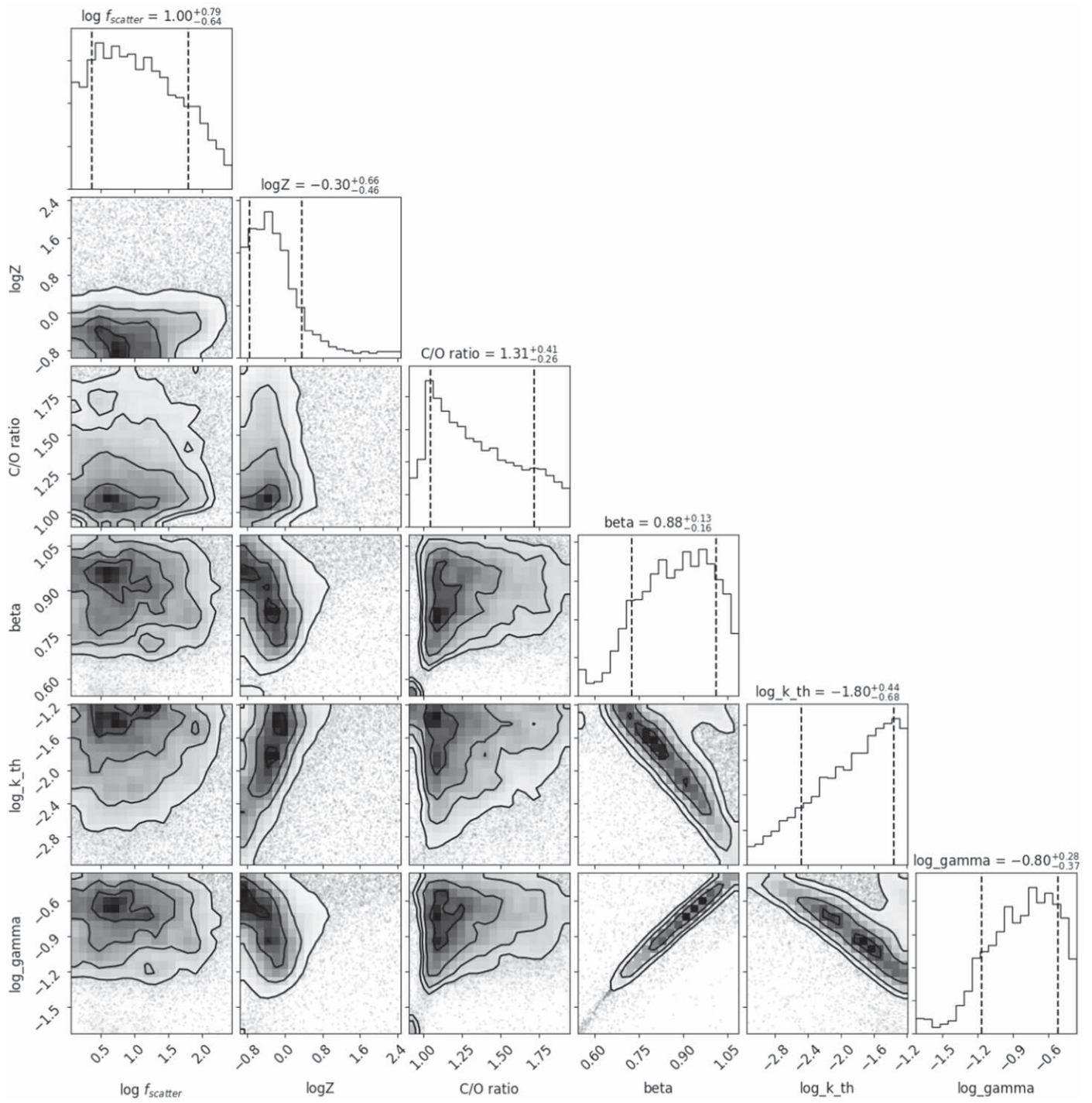


Figure 17. Posterior distribution of PLATON retrieval on the eclipse spectrum.

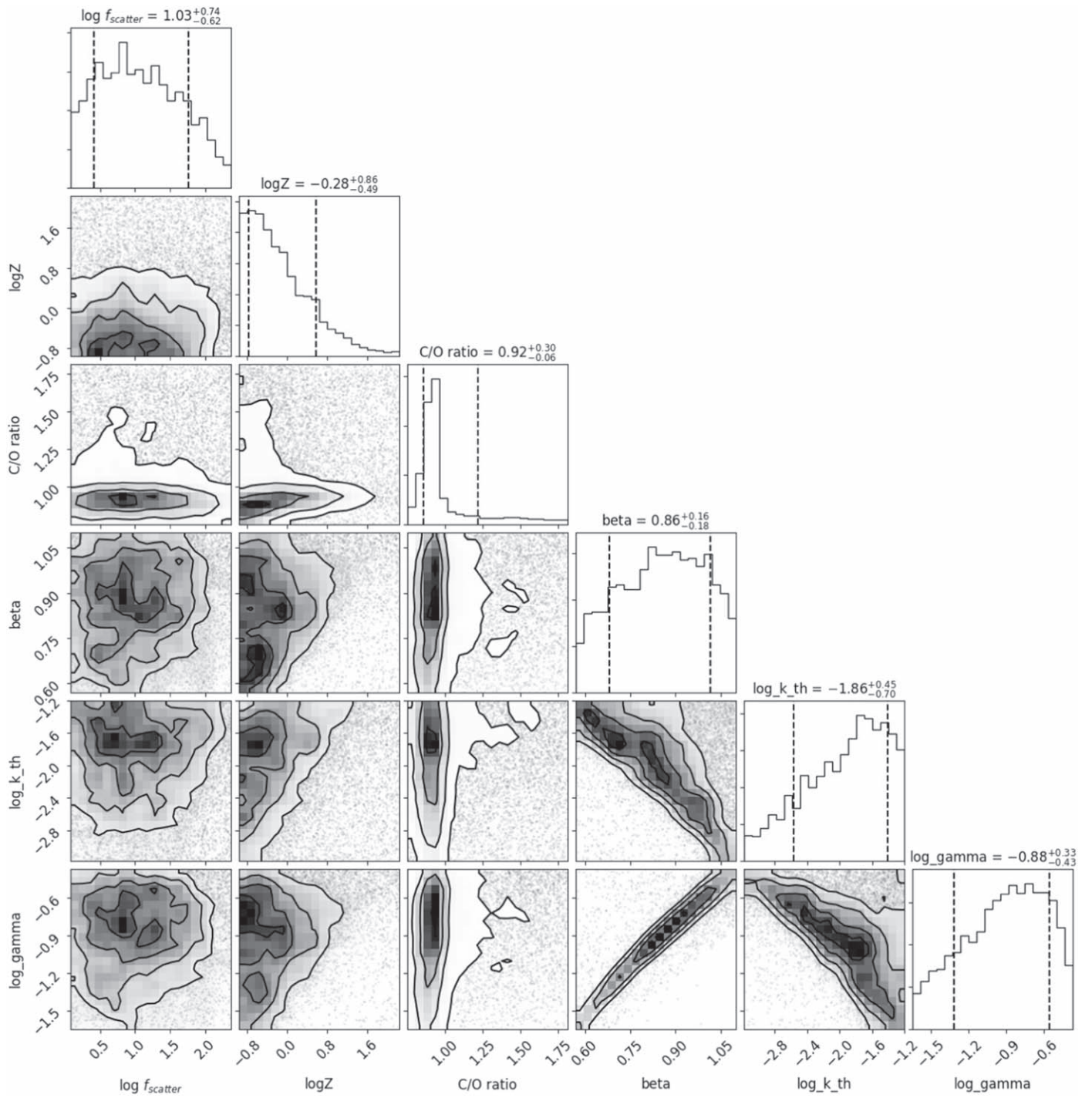


Figure 18. Posterior distribution of PLATON retrieval on the eclipse spectrum without the Spitzer $3.6 \mu\text{m}$ point.

Table 8
WASP-74b Transit Spectrum

Wavelength Midpoint (μm)	Bin Width (μm)	R_p/R_s	R_p/R_s Uncertainty
0.330	0.0400	0.0968	0.001516
0.382	0.0125	0.0931	0.001286
0.403	0.0082	0.0951	0.001172
0.418	0.0069	0.0964	0.000934
0.438	0.0125	0.0959	0.000745
0.455	0.0050	0.0950	0.001013
0.465	0.0050	0.0950	0.000868
0.475	0.0050	0.0959	0.000803
0.485	0.0050	0.0960	0.000705
0.495	0.0050	0.0956	0.000694
0.505	0.0050	0.0965	0.000807
0.515	0.0050	0.0950	0.000749
0.525	0.0050	0.0972	0.000655
0.535	0.0050	0.0953	0.000738
0.545	0.0050	0.0953	0.000743
0.555	0.0050	0.0944	0.000738
0.560	0.0100	0.0923	0.000937
0.565	0.0050	0.0960	0.000748
0.579	0.0089	0.0949	0.000797
0.589	0.0012	0.0964	0.002440
0.605	0.0148	0.0942	0.000749
0.625	0.0050	0.0964	0.001160
0.637	0.0075	0.0954	0.000921
0.652	0.0075	0.0964	0.001451
0.670	0.0100	0.0958	0.000948
0.690	0.0100	0.0951	0.000946
0.710	0.0100	0.0966	0.001130
0.733	0.0125	0.0969	0.000826
0.755	0.0098	0.0958	0.000977
0.769	0.0047	0.0976	0.001994
0.788	0.2425	0.0951	0.000368
0.791	0.0190	0.0960	0.000856
0.830	0.0200	0.0958	0.001150
0.875	0.0250	0.0946	0.001138
0.965	0.0650	0.0939	0.001373
1.119	0.0093	0.0952	0.000404
1.138	0.0093	0.0940	0.000406
1.156	0.0093	0.0943	0.000401
1.175	0.0093	0.0940	0.000392
1.194	0.0093	0.0943	0.000384
1.212	0.0093	0.0946	0.000375
1.231	0.0093	0.0943	0.000371
1.249	0.0093	0.0943	0.000370
1.268	0.0093	0.0948	0.000371
1.287	0.0093	0.0942	0.000367
1.305	0.0093	0.0939	0.000373
1.324	0.0093	0.0943	0.000369
1.342	0.0093	0.0949	0.000368
1.361	0.0093	0.0951	0.000377
1.380	0.0093	0.0949	0.000386
1.398	0.0093	0.0952	0.000374
1.417	0.0093	0.0947	0.000371
1.435	0.0093	0.0947	0.000382
1.454	0.0093	0.0943	0.000379
1.473	0.0093	0.0940	0.000391
1.491	0.0093	0.0952	0.000395
1.510	0.0093	0.0943	0.000403
1.528	0.0093	0.0938	0.000407
1.547	0.0093	0.0942	0.000406
1.566	0.0093	0.0944	0.000411
1.584	0.0093	0.0945	0.000426
1.603	0.0093	0.0951	0.000436
1.621	0.0093	0.0951	0.000433
3.600	0.3800	0.0922	0.000369
4.500	0.5600	0.0938	0.000448

(This table is available in machine-readable form.)

Table 9
Transit Spectrum LD Coefficients

Wavelength Midpoint (μm)	C1	C2	C3	C4
0.330	0.2705	0.3265	0.6655	-0.3603
0.382	0.4105	0.0432	0.8133	-0.3888
0.403	0.3063	0.3801	0.4784	-0.2826
0.418	0.2976	0.4093	0.3791	-0.2082
0.438	0.4077	0.3480	0.2256	-0.1518
0.455	0.3666	0.2493	0.5645	-0.3223
0.465	0.3696	0.3956	0.2662	-0.1798
0.475	0.3562	0.5642	-0.0569	-0.0223
0.485	0.4561	0.4177	0.0456	-0.0988
0.495	0.4121	0.4911	-0.0624	-0.0201
0.505	0.4444	0.3578	0.0620	-0.0501
0.515	0.3952	0.3677	0.1715	-0.1388
0.525	0.4643	0.3587	0.0349	-0.0625
0.535	0.4823	0.3079	0.1146	-0.1165
0.545	0.4839	0.3177	0.0417	-0.0598
0.555	0.5090	0.2242	0.1408	-0.0968
0.560	0.5141	0.2312	0.1016	-0.0735
0.565	0.5190	0.2377	0.0652	-0.0518
0.579	0.5348	0.2233	0.0450	-0.0415
0.589	0.5811	-0.0467	0.5043	-0.2957
0.605	0.5625	0.1408	0.1077	-0.0683
0.625	0.5922	0.0536	0.1836	-0.1021
0.637	0.5855	0.0663	0.1626	-0.0940
0.652	0.6241	0.0128	0.1621	-0.0985
0.670	0.6058	0.0120	0.1747	-0.0921
0.690	0.6179	-0.0367	0.2073	-0.1001
0.710	0.6250	-0.0672	0.2241	-0.1041
0.733	0.6208	-0.0718	0.2233	-0.1084
0.755	0.6350	-0.1154	0.2477	-0.1146
0.769	0.6357	-0.1366	0.2639	-0.1211
0.788	0.6053	-0.0234	0.1975	-0.0987
0.791	0.6397	-0.1459	0.2567	-0.1149
0.830	0.6343	-0.1428	0.2275	-0.1000
0.875	0.6555	-0.2478	0.3210	-0.1341
0.965	0.6439	-0.2223	0.2747	-0.1175
1.119	0.6370	-0.2190	0.1870	-0.0668
1.138	0.6340	-0.2280	0.1960	-0.0718
1.156	0.6280	-0.1970	0.1500	-0.0514
1.175	0.6390	-0.2200	0.1660	-0.0594
1.194	0.6250	-0.1740	0.1070	-0.0324
1.212	0.6280	-0.1790	0.0984	-0.0258
1.231	0.6290	-0.1670	0.0776	-0.0201
1.249	0.6350	-0.1770	0.0841	-0.0242
1.268	0.6390	-0.1690	0.0600	-0.0120
1.287	0.6680	-0.2030	0.0294	0.0052
1.305	0.6460	-0.1590	0.0220	0.0075
1.324	0.6520	-0.1700	0.0268	0.0075
1.342	0.6630	-0.1770	0.0152	0.0147
1.361	0.6660	-0.1820	0.0128	0.0171
1.380	0.6910	-0.2130	0.0192	0.0190
1.398	0.7010	-0.2280	0.0178	0.0241
1.417	0.7210	-0.2570	0.0378	0.0165
1.435	0.7290	-0.2800	0.0469	0.0187
1.454	0.7500	-0.3260	0.0930	-0.0039
1.473	0.7880	-0.3770	0.1120	-0.0026
1.491	0.7960	-0.4150	0.1440	-0.0102
1.510	0.8280	-0.4930	0.2160	-0.0380
1.528	0.8600	-0.5370	0.2280	-0.0310
1.547	0.8810	-0.6060	0.2970	-0.0573
1.566	0.8890	-0.6450	0.3380	-0.0694
1.584	0.8270	-0.5490	0.2740	-0.0540
1.603	0.9480	-0.8340	0.5450	-0.1550
1.621	0.9440	-0.7890	0.4750	-0.1210
3.600	0.4958	-0.4478	0.3558	-0.1170
4.500	0.4255	-0.3651	0.2867	-0.0945













(This table is available in machine-readable form.)

Table 10
WASP-74b Eclipse Spectrum

Wavelength Mid-point (μm)	Bin Width (μm)	Occultation Depth (ppm)	Uncertainty (ppm)
1.1193	0.0093	372	76
1.1379	0.0093	302	73
1.1564	0.0093	284	74
1.1751	0.0093	385	70
1.1937	0.0093	346	68
1.2123	0.0093	246	70
1.2309	0.0093	473	69
1.2494	0.0093	247	67
1.2681	0.0093	460	68
1.2867	0.0093	426	70
1.3053	0.0093	326	67
1.3238	0.0093	365	69
1.3424	0.0093	452	68
1.3611	0.0093	442	73
1.3797	0.0093	418	67
1.3982	0.0093	513	69
1.4168	0.0093	224	63
1.4354	0.0093	427	68
1.4541	0.0093	529	71
1.4727	0.0093	373	71
1.4912	0.0093	431	87
1.5098	0.0093	448	74
1.5284	0.0093	465	75
1.5471	0.0093	574	75
1.5656	0.0093	506	75
1.5842	0.0093	659	79
1.6028	0.0093	624	79
1.6214	0.0093	489	85
3.6000	0.3800	1430	81
4.5000	0.5600	1820	85

(This table is available in machine-readable form.)

ORCID iDs

Guangwei Fu  <https://orcid.org/0000-0002-3263-2251>
 Erin May  <https://orcid.org/0000-0002-2739-1465>
 Kevin Stevenson  <https://orcid.org/0000-0002-7352-7941>
 David K. Sing  <https://orcid.org/0000-0001-6050-7645>
 Joshua D. Lothringer  <https://orcid.org/0000-0003-3667-8633>
 Nikolay Nikolov  <https://orcid.org/0000-0002-6500-3574>
 Thomas Mikal-Evans  <https://orcid.org/0000-0001-5442-1300>
 Vincent Bourrier  <https://orcid.org/0000-0002-9148-034X>
 Leonardo A. dos Santos  <https://orcid.org/0000-0002-2248-3838>
 Munazza K. Alam  <https://orcid.org/0000-0003-4157-832X>
 Gregory W. Henry  <https://orcid.org/0000-0003-4155-8513>
 Mercedes López-Morales  <https://orcid.org/0000-0003-3204-8183>

References

- Alam, M. K., López-Morales, M., Nikolov, N., et al. 2020, *AJ*, 160, 51
 Arcangeli, J., Desert, J.-M., Parmentier, V., et al. 2019, *A&A*, 625, A136
 Baxter, C., Désert, J.-M., Tsai, S.-M., et al. 2021, *A&A*, 648, A127
 Campo, C. J., Harrington, J., Hardy, R. A., et al. 2011, *ApJ*, 727, 125
 Colón, K. D., Kreidberg, L., Welbanks, L., et al. 2020, *AJ*, 160, 280
 Cubillos, P., Harrington, J., Madhusudhan, N., et al. 2013, *ApJ*, 768, 42
 Deming, D., & Knutson, H. 2020, *NatAs*, 4, 453
 Deming, D., Knutson, H., Kammer, J., et al. 2015, *ApJ*, 805, 132
 Evans, T. M., Sing, D. K., Kataria, T., et al. 2017, *Natur*, 548, 58
 Fazio, G. G., Hora, J. L., Allen, L. E., et al. 2004, *ApJS*, 154, 10
 Fu, G., Deming, D., Knutson, H., et al. 2017, *ApJL*, 847, L22
 Fu, G., Deming, D., Lothringer, J., et al. 2021, *AJ*, 162, 108
 Gao, P., Thorngren, D. P., Lee, G. K. H., et al. 2020, *NatAs*, 4, 951
 Garhart, E., Deming, D., Mandell, A., et al. 2020, *AJ*, 159, 137
 Hellier, C., Anderson, D. R., Collier Cameron, A., et al. 2015, *AJ*, 150, 18
 Henry, G. W., Fekel, F. C., & Henry, S. M. 2011, *AJ*, 142, 39
 Henry, G. W., Marcy, G. W., Butler, R. P., & Vogt, S. S. 2000, *ApJL*, 529, L41
 Kataria, T., Sing, D. K., Lewis, N. K., et al. 2016, *ApJ*, 821, 9
 Kreidberg, L. 2015, *PASP*, 127, 1161
 Kreidberg, L., Line, M. R., Thorngren, D., Morley, C. V., & Stevenson, K. B. 2018, *ApJL*, 858, L6
 Lewis, N. K., Wakeford, H. R., MacDonald, R. J., et al. 2020, *ApJL*, 902, L19
 Line, M. R., Wolf, A., Zhang, X., et al. 2013, *ApJ*, 775, 137
 Lothringer, J. D., Barman, T., & Koskinen, T. 2018, *ApJ*, 866, 27
 Lothringer, J. D., Fu, G., Sing, D. K., & Barman, T. S. 2020, *ApJL*, 898, L14
 Luque, R., Casasayas-Barris, N., Parviainen, H., et al. 2020, *A&A*, 642, A50
 MacDonald, R. J., Goyal, J. M., & Lewis, N. K. 2020, *ApJL*, 893, L43
 Madhusudhan, N. 2012, *ApJ*, 758, 36
 Magic, Z., Chiavassa, A., Collet, R., & Asplund, M. 2015, *A&A*, 573, A90
 Mancini, L., Southworth, J., Molliere, P., et al. 2019, *MNRAS*, 485, 5168
 Mandel, K., & Agol, E. 2002, *ApJL*, 580, L171
 May, E. M., Komacek, T. D., Stevenson, K. B., et al. 2021, *AJ*, 162, 158
 May, E. M., & Stevenson, K. B. 2020, *AJ*, 160, 140
 Moses, J. I., Madhusudhan, N., Visscher, C., & Freedman, R. S. 2013, *ApJ*, 763, 25
 Muñoz, A. G., & Isaak, K. G. 2015, *PNAS*, 112, 13461
 Nikolov, N., Sing, D. K., Pont, F., et al. 2014, *MNRAS*, 437, 46
 Öberg, K. I., Murray-Clay, R., & Bergin, E. A. 2011, *ApJL*, 743, L16
 Oswalt, T. D. 2003, in *The Future of Small Telescopes In The New Millennium*, Volume II, The Telescopes We Use, Astrophysics and Space Science Library, Vol. 288, ed. T. D. Oswalt (Dordrecht: Kluwer)
 Parmentier, V., Fortney, J. J., Showman, A. P., Morley, C., & Marley, M. S. 2016, *ApJ*, 828, 22
 Parmentier, V., Line, M. R., Bean, J. L., et al. 2018, *A&A*, 617, A110
 Paulson, D. B., Cochran, W. D., & Hatzes, A. P. 2004, *AJ*, 127, 3579
 Queloz, D., Henry, G. W., Sivan, J. P., et al. 2001, *A&A*, 379, 279
 Sheppard, K. B., Welbanks, L., Mandell, A., et al. 2021, *AJ*, 161, 51
 Showman, A. P., Fortney, J. J., Lian, Y., et al. 2009, *ApJ*, 699, 564
 Sing, D. K., Fortney, J. J., Nikolov, N., et al. 2016, *Natur*, 529, 59
 Sing, D. K., Lavvas, P., Ballester, G. E., et al. 2019, *AJ*, 158, 91
 Sing, D. K., Pont, F., Aigrain, S., et al. 2011, *MNRAS*, 416, 1443
 Sing, D. K., Wakeford, H. R., Showman, A. P., et al. 2015, *MNRAS*, 446, 2428
 Stevenson, K. B., Desert, J.-M., Line, M. R., et al. 2014, *Sci*, 346, 838
 Stevenson, K. B., & Fowler, J. 2019, Instrument Science Report, WFC3 2019-12
 Stevenson, K. B., Harrington, J., Fortney, J. J., et al. 2012, *ApJ*, 754, 136
 Wallack, N. L., Knutson, H. A., & Deming, D. 2021, *AJ*, 162, 36
 Zhang, M., Chachan, Y., Kempton, E. M.-R., et al. 2020, *ApJ*, 899, 27
 Zhang, M., Knutson, H. A., Kataria, T., et al. 2018, *AJ*, 155, 83
 Zhou, Y., Apai, D., Lew, B. W. P., & Schneider, G. 2017, *AJ*, 153, 243